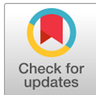

Research Article | Vol. 30, No. 17 / 15 Aug 2022 / Optics Express 30246

Optics EXPRESS

Integrated optical device for Structured Illumination Microscopy

MATTEO CALVARESE,[1] PETRA PAIÈ,[1,2] ALESSIA CANDEO,[2] GIANMARIA CALISESI,[2] FRANCESCO CECCARELLI,[1] GIANLUCA VALENTINI,[1,2] ROBERTO OSELLAME,[1] HAI GONG,[3] MARK NEIL,[3] FRANCESCA BRAGHERI,[1] AND ANDREA BASSI[1,2,*]

[1] *Istituto di Fotonica e Nanotecnologie (IFN), Consiglio Nazionale delle Ricerche (CNR), Piazza Leonardo da Vinci 32, 20133 Milan, Italy*
[2] *Dipartimento di Fisica, Politecnico di Milano, Piazza Leonardo da Vinci 32, 20133 Milan, Italy*
[3] *Department of Physics, Imperial College London, South Kensington Campus London SW7 2AZ, UK*
[*] *andrea1.bassi@polimi.it*

Abstract: Structured Illumination Microscopy (SIM) is a key technology for high resolution and super-resolution imaging of biological cells and molecules. The spread of portable and easy-to-align SIM systems requires the development of novel methods to generate a light pattern and to shift it across the field of view of the microscope. Here we show a miniaturized chip that incorporates optical waveguides, splitters, and phase shifters, to generate a 2D structured illumination pattern suitable for SIM microscopy. The chip creates three point-sources, coherent and controlled in phase, without the need for further alignment. Placed in the pupil of a microscope's objective, the three sources generate a hexagonal illumination pattern on the sample, which is spatially translated thanks to thermal phase shifters. We validate and use the chip, upgrading a commercial inverted fluorescence microscope to a SIM setup and we image biological sample slides, extending the resolution of the microscope.

© 2022 Optica Publishing Group under the terms of the Optica Open Access Publishing Agreement

1. Introduction

Structured Illumination Microscopy (SIM) is an optical technique that is becoming of widespread use for imaging at high resolution and beyond the classical diffraction limit [1]. Initially used for obtaining optical sectioning [2], SIM is now commonly and commercially used for super-resolution microscopy. Structured illumination microscopy can double the resolution of a diffraction limited microscope [3], if it is implemented with linear excitation, where the fluorescence emission is proportional to the excitation intensity. It can further increase the resolution down to the tens of nanometer scale [4], if operated in a nonlinear regime. Recently, structured illumination has opened new possibilities in three-dimensional localization microscopy [5], light sheet microscopy [6] and far field optical nanoscopy [7], among others.

The generation of a coherent SIM pattern is commonly achieved by interference of two or more laser beams on the sample. In an epifluorescence microscope, a sinusoidal pattern can be generated by focusing two coherent laser beams into the pupil of the microscope. By changing the relative phase of beams, the pattern moves (spatially shifts) through the field of view. In its original implementation [3], a diffraction grating created the two coherent beams, and a mechanical translator (and rotator) was used to change the pattern spatial phase and angle. In recent SIM applications the beam is shaped with a spatial light modulator [8,9]. This approach has the advantage to allow the creation of complex modulation patterns, with high phase precision, moreover the spatial light modulator can be further used to measure the microscope aberrations [10]. However, even in modular implementation [11] a bulk optical setup for SIM pattern generation has the disadvantage to be cumbersome and to require day-by-day adjustments. Recently, a few methods to generate a SIM pattern, based on optical fibers and (temporal) phase

#466225 https://doi.org/10.1364/OE.466225
Journal © 2022 Received 8 Jun 2022; revised 8 Jul 2022; accepted 8 Jul 2022; published 2 Aug 2022

modulation have been proposed [12,13], but a fully integrated optical system that does not require free space elements is still lacking.

Integration of the SIM pattern generator could be obtained with femtosecond laser micromaching (FLM) [14], a well-established microfabrication technique that exploits fs-pulsed laser irradiation on transparent or absorptive materials to selectively change their structural and optical properties. The material modifications depend on the irradiation parameters and, among the possible changes, a localized increase in refractive index can be induced with respect to the pristine material. This allows the realization of optical waveguides, with controlled birefringence, ideal for polarization manipulation [15]. Using metal deposition and exploiting thermo-optic effects, phase shifters can be built on the optical circuits obtained with FLM, with switching response that can be as low as 200 μs [16], potentially allowing > kHz switching rate. It is worth noting that although this approach is 10 times slower than fiber-based modulation [12], in typical SIM measurements the acquisition time is limited by the fluorescence signal reaching the camera and the kHz switching rates are beyond what is typically required with scientific CMOS image acquisitions.

Here we present an integrated device for patterned illumination that can be used as a light source for SIM microscopy. The device consists of a miniaturized glass chip fabricated by FLM that incorporates optical waveguides, beam splitters and thermal phase shifters. The light coupled into the input waveguide of the chip is split into three waveguides at its output. The relative phases of the three waveguides are controlled by a voltage applied to the thermal shifters. Three optical fibers are connected to the waveguides at the output of the chip and their other ends are placed on a glass ferrule, positioned at the vertices of an equilateral triangle. Each fiber core is thus 120° apart from the others. These three point-sources, azimuthally polarized, interfere at the sample, producing a hexagonal intensity pattern, suitable for SIM microscopy [17,18], specifically in its hex-SIM implementation [9]. The hex-SIM approach consists in illuminating the sample with a hexagonal pattern, which can be created by aligning three coherent laser beams on the objective pupil. The pattern must be shifted laterally along a straight line and only 7 images are required to deduce an enhanced resolution image, without the need of pattern rotation, typical of conventional SIM. Here, by controlling the relative phase of the three waveguides, the patterns are shifted on the sample, acquiring the 7 images required for hex-SIM reconstruction.

2. Results and discussion

2.1. Chip layout

Our device is constructed as a glass-based optical circuit that splits the laser light, coupled to the chip, into three output beams (Fig. 1). The use of FLM on glass is one of the possible techniques for manufacturing such photonics devices in the visible range. Another common technology involves the use of optical circuits based on silicon nitride (Si_3N_4), which enables the creation of waveguides with high refractive index. The silicon nitride technology is indeed ideal for total internal reflection microscopy [19] but due to large coupling losses it is less suitable for far field illumination. Conversely, the use of FLM on glass allows the manufacturing of waveguides with small refractive index variations, which can be easily coupled with standard optical fibers.

The developed optical circuit is composed of two integrated couplers, which act as beam splitters and distribute laser light among the three output waveguides, according to their coupling ratio. Laser light is coupled into one waveguide through a polarization maintaining (PM) fiber. The first splitter is designed with a coupling ratio of 33%, one third of the initial power continues travelling in the first arm, while the remaining is guided to the second splitter. The latter is designed as a 3 dB coupler, with a coupling ratio of 50%. With such power splitting, the initial power is, ideally, equally distributed among the three output ports. In our device we found that the power ratio at the three outputs was 33%, 36% and 30%.

Optics EXPRESS

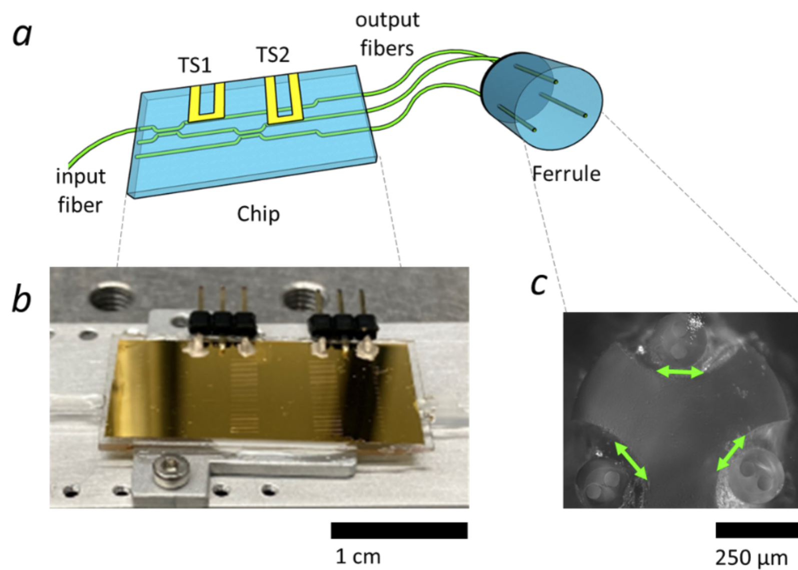

Fig. 1. (a) Rendering of the integrated optical circuit with two metal thermal phase shifters (TS1 and TS2) positioned on the waveguides fabricated in the glass chip. (b) Picture of the chip with pins for electrical connection. (c) Picture of the ferrule. The 3 polarization maintaining output fibers are placed at the vertexes of an equilateral triangle inscribed in a circumference corresponding to the ferrule border. The two small circles in the fiber facet indicate one of the two perpendicular axis of the PM fibers that maintain the polarization. In green the expected polarization state when the input polarization is coupled perpendicular to the line connecting the circles.

It is worth noting that the optical waveguides fabricated with FLM are slightly birefringent, with the main axis parallel to the FLM writing beam direction [15]. This is due to the ellipticity of the waveguide cross-section and to the mechanical stress induced in the modified region. Thus, the polarized light from the PM input fiber is maintained throughout the chip.

The optical circuit is integrated with two thermal shifters (TS1 and TS2 in Fig. 1(a)) to control the relative phase of the guided beams [16]. The shifters create a phase difference φ_{ij} between each pair of guided beams *i,j* and they are constituted of a thin metal resistor which is placed on top of one arm of each beam splitter. An applied voltage across them, causes a power dissipation into the chip substrate, and a consequent refractive index difference between the beam paths by thermo-optic effect. This gives a phase shift between two adjacent beams. Using two thermal phase shifters is enough to control the relative phases of the three beams.

The three outputs of the chip are coupled and glued to a PM fiber array, which ends into a custom designed ferrule. The three fibers tips are arranged in a triangular configuration and their optical axes are aligned before gluing, finely positioning them in azimuthal polarization configuration (Fig. 1(c)). As a result, the device creates a three-beam source with the desired polarization without the need for additional bulk optical elements. The fabrication of both the active photonic chip and ferrule is based on femtosecond laser micromachining (see Materials and Methods).

2.2. *Structured illumination microscope*

The three-points at the ferrule plane act as the source for the pattern. Thanks to the Fourier transforming properties of lenses, imaging the three coherent points in the back focal plane of a lens, produces a hexagonal intensity pattern in its front focal plane [17]. We initially characterized

Optics EXPRESS

the pattern placing the ferrule in front of a plano-convex 50 mm lens. This configuration creates an interference pattern which can be collected by a camera placed in the focal plane of the lens (Fig. 2(a)). As expected, the pattern shows hexagonal symmetry with clear minima. We evaluated its contrast as described in the Materials and Methods in the center of the pattern, obtaining C = 0.63 (with C= 0.74 if we consider only the absolute maximum and the minimum values of the pattern profile shown in Fig. 2(b)), which is lower than the theoretical value (unity). We believe that this contrast loss is due to the non-perfect positioning of the optical fibers on the ferrule, non-perfect polarization coupling and non-ideal alignment of the PM fibers. Instead, the contrast should not be affected by loss of coherence in the optical fibers, whose length (~10 cm) is an order of magnitude shorter than the coherence length of the laser.

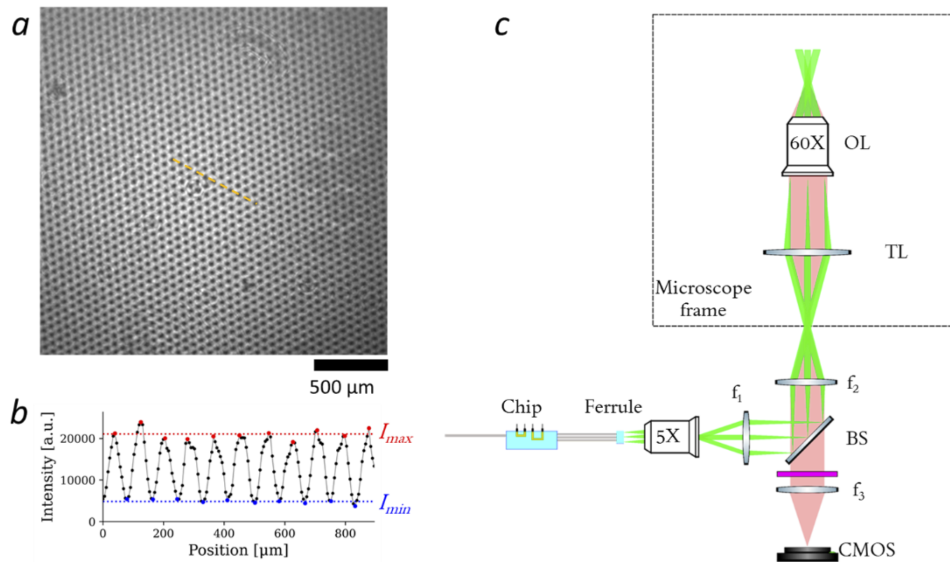

Fig. 2. (a) Hexagonal pattern formed by focusing the three-point sources from the ferrule plane to a camera, using a 50 mm lens (b) Profile of the pattern, corresponding to the dotted yellow line in panel *a*, highlighting the values used to calculate the contrast. (c) Structured illumination microscope. Green beams represent the excitation while pale red the emitted fluorescence. The dashed line delineates the inverted microscope frame. The chip is connected with polarization maintaining fibers to the ferrule. A low NA objective (5X), together with the first lens (f_1 = 150 mm) image the three fibre facets at the ferrule plane onto the dichroic mirror / beam splitter (BS). The second lens (f_2 = 150 mm) with the tube lens (TL) of the inverted microscope bring this image to the back focal plane of the microscope objective. The microscope objective (60X) creates the pattern on the sample plane of the microscope. The emitted light is collected by the objective and imaged at the output port of microscope where a relay system formed by lens 2 and lens 3 (f_3 = 150 mm), creates a secondary image at the CMOS camera. A bandpass filter (BF) eliminates the excitation light from the detection path.

We then aimed to create an image of the three point-sources in the microscope's pupil, so to generate the hexagonal pattern in the object plane. In a commercial inverted microscope this is possible by adding a lens in front of the ferrule, that in combination with the tube lens (TL) of the microscope forms a magnified image of the point sources. We selected this lens to be a 5X microscope objective (Mitutoyo, LWD, Plan Apo, 0.14 NA) and we mounted the chip with the ferrule on a 3-axis stage to facilitate the alignment of the three point-sources in the optical path. To have more flexibility on the alignment of the illumination and detection path, we added

Optics EXPRESS

a telescope at the output port of the microscope, composed of two 150 mm lenses (f1 and f2 in Fig. 2).

The three point-sources defined a triangle inscribed in a circle with radius 0.25 mm at the ferrule plane and the circle was magnified to a 1.25 mm radius at the back focal plane of the objective. The pattern period at the sample plane depends on the illumination objective used to form the pattern, its value is affected both by the numerical aperture and the physical size of the pupil. We can in fact define a filling factor FF, as the ratio between the radius of the circle containing the three points in the back focal plane and the pupil radius. The higher this value is, the closer the pattern period gets to the theoretical maximum resolution of the objective.

We used an 60X oil-immersion objective (Olympus, Plan-Apo, 1.4 NA). In this configuration, we had a filling factor of ∼0.5, which corresponds to a pattern period of ∼450 nm. The filling factor (FF) determines the resolution improvement of the SIM reconstruction, as for hex-SIM the resolution can be estimated as $\Delta\rho_{SIM} = \frac{\Delta\rho_{WF}}{1+FF\sqrt{3}/2}$ where $\Delta\rho_{WF}$ is the widefield resolution, limited by the microscope objective lens. In the best case the filling factor is 1 and the resolution improvement is 1.87. We tested a filling factor of 0.5, in order to have a clearly visible pattern at the image plane and to demonstrate that the technique is able to generate and move the pattern precisely. Considering that the waist of the beam at the fibers plane is 2.7 µm, at the pupil the waist of each of the sources is 13.5 µm, giving rise to a modulation area with a diameter of ∼ 60 µm (FWHM), at the object.

Figure 3(a) shows a fluorescent cell (from Invitrogen FluoCells #1 slides labelled with MitoTracker Red), illuminated with the pattern. The hexagonal lattice is superimposed to the fluorescence signal. Consequently, the Fourier power spectrum of the image (Fig. 3(b)) has 7 peaks, clearly visible at low filling factors, consisting in the continuous component of the illumination intensity (central peak) plus 6 peaks due to the modulation. Thus, the hex-SIM pattern can be seen as the combination of three 1D sinusoidal patterns modulated at three different carrier frequencies (highlighted in red in Fig. 3(b)).

We proved that a controlled shift of the pattern on the cell is possible, by applying different consecutive voltages to the thermal shifters, and recording the corresponding images. Figure 3(c) and Fig. 3(d) show a subsection of the cell, acquired with two different values of phase shifts. In the line plot of Fig. 3(e), the pattern translation in the sample plane is visible. This measurement indicates that the chip allows the generation of a SIM pattern on the object plane of the microscope that can be spatially translated in the sample plane by changing the relative phase of the output beams.

2.3. Phase shift and calibration

The hexagonal pattern with active phase control allows one to perform demodulation and to reconstruct super-resolved images acquiring N = 7 images with a well precise combination of relative phases between the three laser beams [9]. One advantage of hex-SIM consists in having a number of images for reconstruction smaller than the number of images required for standard SIM (i.e., 9 acquisitions corresponding to 3 spatial phases and 3 angles). To implement the N desired phase shifts (see Materials and Methods), we first performed a calibration of the thermal shifters' response, to assess the voltage-to-phase shift characteristics and find the correct values of input signals. Voltage calibration was performed in a pre-assembling step of the chip, before the output PM fibers were glued. Light was coupled into the chip input and the far field interference pattern of two beams at a time is collected by a camera, while voltage is scanned in a suitable range (0-9 V). From post processing of the acquired images, a characteristics curve is obtained, one for each thermal shifter (Fig. 4(a)).

Nevertheless, the precision of this calibration method is not ideal. The reliability of the analogue voltage source, the manual change of the voltage levels and the following gluing process are some of the factors that may affect the final precision of the phase shifting process. Inaccurate

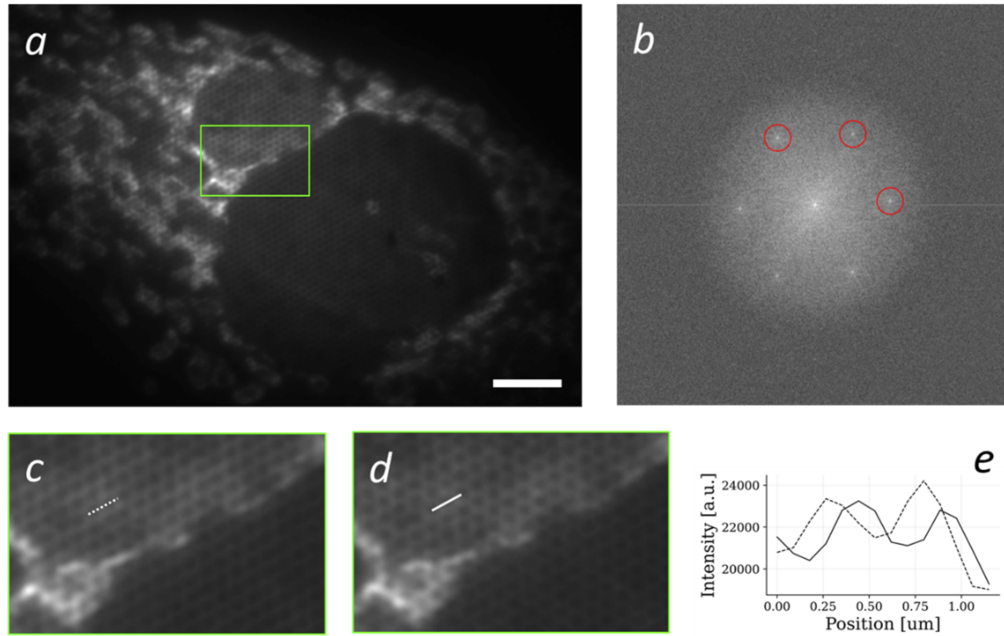

Fig. 3. Illumination pattern formation and translation. (a) Illumination pattern formed on a fluorescent cell with a 60X/1.4NA oil immersion objective. The pattern period is ca. 450 nm. Scale bar is 5 µm. (b) Power spectrum (logarithmic scale) of the image in panel *a*, showing 7 peaks due to the presence of the pattern. The red circles highlight the carrier frequencies of the SIM pattern. (c) and (d) zoomed area from panel *a* acquired with different voltages applied to the thermal shifters. (e) Line plot from the white lines of panel *c* (dotted) and *d* (solid). The line plot shows the effective translation of the illumination pattern.

phase shifts may result in artefact in the reconstructed image. To circumvent this problem, we implemented a self-calibration method, that exploits an iterative process to calibrate the voltage signals. Initially, images are acquired using the voltage signals found in the analogue calibration, then the phases are calculated from the N acquired images using autocorrelation-based methods (see Material and Methods). The error ϵ_{ij} between the expected phases and the measured values, for each pattern, is computed as:

$$\epsilon_{ij} = \frac{\Delta\varphi_{ij}^{exp} - \Delta\varphi_{ij}^{meas}}{\Delta\varphi_{ij}^{exp}} \tag{1}$$

Here the indexes i an j indicate a generic couple of beams, thus for each pattern we have 3 error values (i.e. ϵ_{12}, ϵ_{13}, ϵ_{23}).

Depending on the value of the errors, a correction to the two input voltages is applied considering the effect of each thermal shifter to the relative phase shift (see Materials and Methods). The phase shift depends quadratically on the applied voltage, however, as a first approximation a linear correction is made, increasing or decreasing the voltages at each step, according to the errors mentioned before:

$$\begin{cases} V_1^n = V_1^{n-1} + \epsilon_{13}^{n-1} dV_{res} + c\epsilon_{12}^{n-1} dV_{res} \\ V_2^n = V_2^{n-1} + \epsilon_{23}^{n-1} dV_{res} - c\epsilon_{12}^{n-1} dV_{res} \end{cases} \tag{2}$$

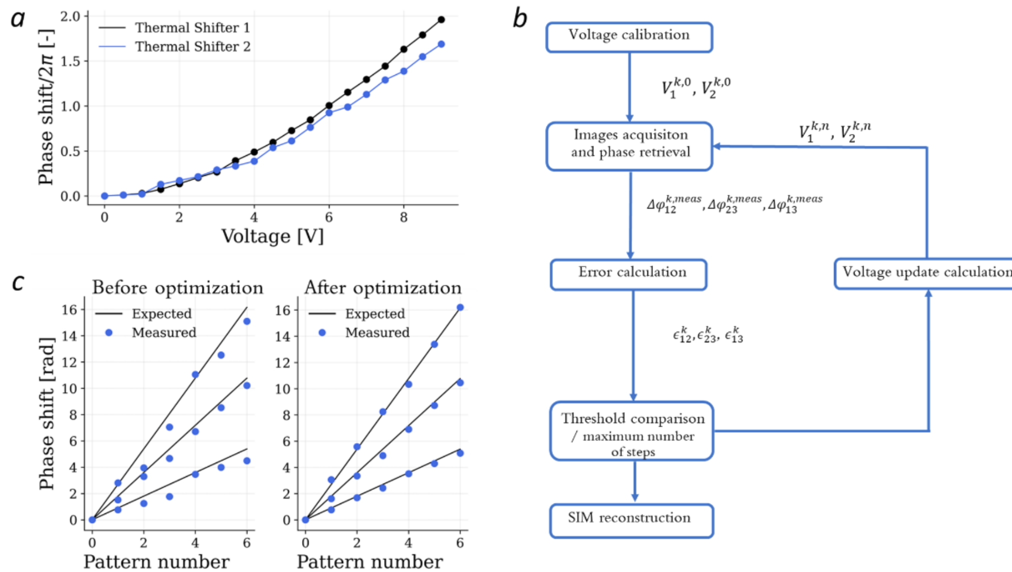

Fig. 4. Phase shift calibration. (a) Pre-assembly calibration. The phase shift of two beams is measured while changing the applied voltage to each thermal phase shifter and a voltage-to-phase characteristics is retrieved. (b) Self-calibration block diagram. (c) Comparison between measured (blue dots) and expected (black lines) phase shifts between the three beams before and after 10 cycles of calibration process.

where n is the iteration number, dV_{res} is a voltage step that is set (typically at 0.3 V) at the beginning of the calibration process and it indicates the maximum voltage increase for each iteration, c is a parameter that takes into account for possible asymmetries in the system. Ideally, only the error on $\Delta\varphi_{13}$ and $\Delta\varphi_{23}$ would be enough to set the new voltage values, because $\Delta\varphi_{12}$ is the difference between them. However, possible nonidealities make it convenient to introduce an additional degree of freedom for the reduction of ϵ_{12}. The relation between the voltage and the phase is described in the Materials and Methods. A value of c =0.5 was chosen empirically from the resulting phase reconstruction and typically used in our calibration. Its impact on the phases is however limited, so a precise estimate is not necessary.

The process is repeated until the error meets a suitable threshold or a maximum number of iterations M is reached. It is worth noting that, during the process, the region of interest for the autocorrelation analysis is kept the same, so that phase calculation is consistent within consecutive iterations.

Figure 4(c) shows the comparison between the measured phase shifts for each pattern before and after the calibration process (with M = 10). We observe that the phases applied after the calibration are in good agreement with the theoretical ones (Fig. 4(c), right panel). The average root-mean-square error among the three sets of phases was 0.68 rad (normalised RMS of 16.5%) before optimization and, after 10 cycles of calibration, it was reduced to 0.26 rad (normalised RMS of 5.7%). Once the calibration process is completed, the new voltage signals can be used for the SIM measurement, acquiring N images at the desired phase.

2.4. SIM imaging of biological slides

We imaged a cell slide (FluoCells Prepared Slides #1) using an Olympus 60x/1.4NA oil immersion objective. The 532 nm laser excites the MitoTracker Red CMXRos that was used to stain the mitochondria of the cells. The pattern created on the samples had a period of 380 nm with a

filling factor of 0.57. After the self-calibration process, N = 7 images with the correct phases were acquired and the reconstruction process was performed (see Materials and Methods). Figure 5 compares a widefield image with the reconstruction obtained with SIM. One major effect of SIM reconstruction is the reduction of the background in the image, which significantly improves its contrast, relative to pseudo widefield reconstruction (obtained as the sum of the 7 acquired images). Then, the reconstructed SIM image shows an improved resolution when imaging the mitochondrial membranes. This improvement is particularly visible by taking a line profile of a filament (Fig. 5(d)), that shows a narrower structure in the SIM reconstruction than in the widefield reconstruction. To quantify this resolution improvement, we used a decorrelation analysis previously proposed [20]. We estimate a resolution improvement of 1.5 times, consistent with the used pupil filling factor.

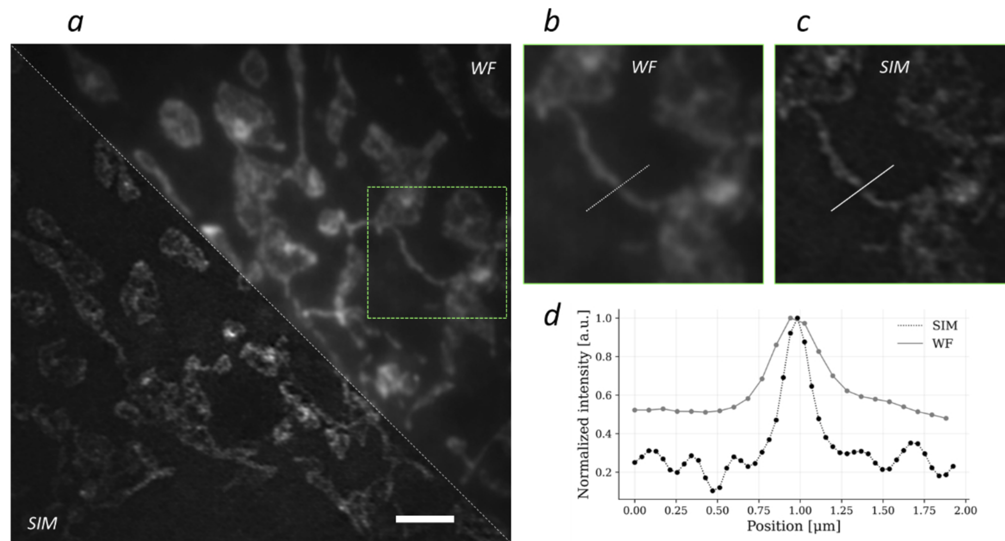

Fig. 5. SIM reconstruction results. (a) Pseudo-widefield (WF) vs SIM reconstruction of a MitoTracker Red CMXRos stained cell. (b) Enlarged detail of the green square of the WF image. (c) Enlarged detail of the SIM image. (d) Line profile of the reconstruction along the white line in panels *b* and *c*. Scale bar is 3 µm.

These measurements show that our device can be used as an add-on system to a standard fluorescence microscope, to implement structured illumination microscopy. So far, the system has been tested at relatively low filling factor (0.5) which is a drawback for some high-resolution SIM applications. However, similar filling factors are used in super-resolution applications [5] and the developed technology can also be of interest for applications where space constraints are present, including multimodal microscopes and miniaturized devices [21,22]. Future work will be dedicated to extending the filling factor along with the numerical aperture, improving the contrast, optimizing the polarization, and increasing the speed of the chip. In addition, broadband directional couplers can be fabricated by proper optimization of their layout (i.e. interaction length, distance between waveguides and curvature radius) [23], offering the possibility to create integrated multicolor SIM pattern generators.

3. Materials and methods

3.1. Illumination and detection optical system

The system starts with a laser (RGB Photonics, 532 nm, 200 mW) coupled into a polarization maintaining (PM) fiber (Thorlabs P3-488PM-FC-2). The fiber is coupled to the chip and fixed

at the input port with a UV curing glue (Optical Adhesive 133 by Norland). The output of the waveguides is coupled and fixed to the PM fiber array (AMS Technologies) and the three fibers are then placed on the triangular ferrule. The typical power at the entrance of the chip was 40 mW and the power on each point source was 2.5 mW. The main source of losses are the fiber connections at the input and output facets of the chip, giving an overall transmission efficiency of about 15%. Yet, reduction of these losses by up to 0.3 dB per facet with standard optical fibers can be obtained on glass chips fabricated with FLM [24]. The absorption (and consequent heating) of the curing glue could be a limitation to the maximum power delivered to the chip, but we have tested the system with laser power up to 150 mW without noticing any damage to the glued connections.

A 5x microscope objective (Mitutoyo, LWD, Plan Apo), together with two 150 mm lenses (Fig. 2) form the hexagonal pattern at the entrance of the microscope port of a Leica DM IRBE inverted microscope. This pattern is brought to the object plane by the tube lens and the microscope objective lens. A dichroic mirror (Semrock FF560-FDi01-25 × 36) reflects the illumination wavelength towards the microscope objective and transmits the emitted light. The mirror is in a plane conjugated with the pupil of the microscope, to facilitate the pattern alignment. Note that the use of a dichroic mirror can degrade the polarization of the SIM beams because the mirror causes a different phase shift on s- and p-polarized light. A possible approach to avoid this problem consists in adding a second dichroic mirror at a 90-degree angle with respect to the first [25]. As an alternative to this approach, in some acquisitions (e.g., data shown in Fig. 3) we used a 30-70 beam splitter (Thorlabs BSS10R), with the drawback of losing a significant fraction of the emitted fluorescence. It is worth noting that a degradation in polarization is reflected in a change in contrast (which is significant at high NA and high filling factors) and potentially in an inversion of the pattern contrast.

The detection path of the microscope includes a relay system with a shared lens (f_1) and a second lens in front of the camera ($f_3 = 200$ mm). A CMOS camera (FLIR Grosshoper) is used for image acquisition and a bandpass filter (Semrock 590/36 nm BrightLine) is used to reduce the residual excitation light.

Phase control is carried out by applying two analogue signals of a National Instruments DAQ board (NI USB-6212), which provide the input voltages to the electrical pins on the chip. A python code was developed, within the Scope Foundry (http://www.scopefoundry.org/) framework, to control the board, acquire the images and process the data.

3.2. Integrated photonic circuit fabrication

The fabrication of the photonic chip consists in different steps. Firstly, the integrated optical circuit was written by FLM in a borosilicate glass substrate (Eagle XG, Corning). We used a Yb:KYW custom-built cavity-dumped mode-locked laser oscillator, with 300 fs long pulses at 1030 nm, and a repetition rate of 1 MHz. An initial characterization of the waveguide losses allowed us to determine the optimal irradiation parameters. We used a 50x objective (Olympus, LCPlan N, 0.65 NA) as focusing objective, an average laser power of 230 mW, a scan velocity of 40 mm/s and a multiscan approach based on 12 overlapping irradiations. Secondly, a previously optimized thermal annealing process, with a peak temperature of 750 °C [24], followed the irradiation. With this process, we obtained single mode waveguides, with propagation losses of about 0.3 dB/cm and symmetric mode dimensions of about $2.7 \times 2.8\ \mu m^2$ for 532 nm wavelength.

To create a balanced three-beam splitter, we fabricated 3 dB directional couplers and we characterized them to find the relationship between coupling ratio and interaction length. The arms distance within the interaction region was fixed to 5 µm. With this characterization, we found the optimal interaction lengths for both the splitters, and we obtained a rather balanced device, with a power ratio at the three outputs of 33%, 36% and 30%. The interaction length was 0.75 mm for the first splitter and 0.48 mm for the second.

Optics EXPRESS

3.3. Thermal shifter fabrication and properties

We designed the coupler geometry and the thermal phase shifters based on a previous work [16], where the temporal dynamics, as well as the power consumption of a similar device, were investigated. To have a short temporal response and a low dissipated power, we have fabricated the splitters at a distance of 15 µm from the glass surface and with a distance of 30 µm between the arms. At the output ports, the waveguides are moved apart to 127 µm, to match the spacing of the PM fibers. To create the thermal phase shifters, a metal deposition process was carried out. First, a 2 nm layer of chromium was deposited over the glass substrate to enhance gold-to-glass adhesion. Then, 100 nm of gold have been deposited using a magnetron sputtering system. Subsequently, a thermal annealing process up to 500°C has been performed to increase the resistor stability over time.

The resistors layout has been obtained by femtosecond laser ablation of the metal layer, using a 10x objective (Leica, 0.25 NA), 200 mW of average laser power and 2 mm/s scan velocity. The two resistors have a length of 3 mm along the beam propagation axis, and a width of 15 µm, and they both show an electrical resistance of about 91 Ω. We also implemented some superficial symmetrical trenches, just besides the resistors, to enhance the dynamic response of the device [16]. The trenches are symmetric, 8 µm deep and around 9 µm wide. Using a stepped analog signal the switching time is in the order of 2 ms, which can be reduced to 200µs applying a pulsed and stepped voltage to the resistors [16]. The stability of electrical resistance is crucial for the one of the induced phase shift. Gold-based resistors have already demonstrated good resistance stability even for continuous operation at high power [26], showing a resistance fluctuation of less than 0.1% after 8 hours and no evidence of short-term drifts. Temperature drifts due to overheating of the substrate are prevented by mounting the device on a metal heat sink with a thermally conductive compound (RS PRO Heat Sink Compound) to maximize the thermal contact. The resistors present low temperature coefficient of resistance (TCR = 0.37%/K) so that the air conditioning system in the room is sufficient to avoid the influence of ambient temperature fluctuations on the phase.

The phase shows a linear dependence with the electric dissipated power, however given the position of the phase shifters on the optical circuit, the applied power at the two shifters influences the phases according to:

$$\begin{cases} \Delta\varphi_{12} = \alpha(P_1 - P_2) \\ \Delta\varphi_{23} = \alpha P_2 \\ \Delta\varphi_{13} = \alpha P_1 \end{cases} \tag{3}$$

where α is a constant, P1 and P2 are the electrical powers applied to thermal shifter 1 and 2 respectively (Fig. 1(a)). The voltage is related to the power by a quasi-quadratic relation because the electrical resistance is not constant when the temperature increases ($P = \frac{V^2}{R(P)}$, where the resistance R is a function of the power P). In the ideal case, an increase in V_1 results in an increase of $\Delta\varphi_{13}$ and $\Delta\varphi_{12}$, but will not affect $\Delta\varphi_{23}$. Instead, V_2 rising decreases $\Delta\varphi_{12}$, increases $\Delta\varphi_{23}$ and leaves $\Delta\varphi_{13}$ unchanged. Therefore, a positive error in $\Delta\varphi_{13}$ (measured value smaller than expected value) means that V_1 must be increased whereas a positive error in $\Delta\varphi_{23}$ is an indicator of a too low V_2. An error in $\Delta\varphi_{12}$, on the other hand, is reflecting both on V_1 and V_2 (See Results and Discussion).

3.4. Ferrule fabrication

The technique employed for the ferrule fabrication is FLICE (femtosecond laser irradiation followed by chemical etching) [14]. It is an established method to realize 3D microstructures in glass materials. FLICE consists in a first fs-laser irradiation to selectively modify the substrate sensitivity to chemical agents, and a consequent chemical bath in an aqueous solution of

Optics EXPRESS

hydrofluoric acid at 20%, which preferentially removes the irradiated region. We used a 2 mm thick fused silica glass (Foctek) and the same laser used for the direct writing of the integrated photonic circuit. However, for the FLICE process we used the laser second harmonic (515 nm), a 63x objective (Zeiss, 0.75 NA) and an average power of 280 mW. Using these laser parameters, we have irradiated the ferrule, defining the profile along the substrate thickness. We started from the bottom layer of the glass and we have reached the top surface by irradiating multiple concentric planes with an inner separation along the vertical direction of 5 µm. The initial circular radius of the ferrule was 285 µm, but after the chemical etching the size is reduced to 250 µm. The positioning of the 3 fibers in the ferrule was performed using a 6-axis stage (PI H-811.I2 6-Axis Miniature Hexapod) to position each fiber in its paired hole on the ferrule and rotate them to the required angle of inclination. Three cameras were used to monitor the process from three different viewpoints (frontal, lateral and from above) to verify the correct alignment. Finally, the fibers were attached to the glass ferrule using a UV-curing glue (Optical Adhesive 133 by Norland) that is cured by a UV led lamp (LC-L2, Hamamatsu) with an emitted power of 250 mW at 365 nm. The accuracy of fiber positioning is limited by the gluing process, because as the glue solidifies it changes its volume and slightly displaces the fibers. In our device we positioned the fibers with less than 10% error relative to the desired locations.

The advantage of using a custom-made ferrule is that we can align the PM fibers into an azimuthal polarization, without the need of additional polarizers along the optical path. The polarization configuration is intrinsically reached by the fibers arrangement.

3.5. Modulation contrast

The modulation depth of a uniform hexagonal pattern can be found from its power spectrum, which presents 7 peaks as the ones shown in Fig. 3(b). It is given by the ratio between the sum of the 6 peaks at the carrier frequencies, and the central peak. This value corresponds to the contrast of the pattern that was evaluated as:

$$C = \frac{I_{MAX} - I_{MIN}}{I_{MAX} + I_{MIN}} \tag{4}$$

Where I_{MAX} and I_{MIN} are the maximum and minimum values of the modulation. We evaluated these quantities as the average values of the peaks and valleys of the pattern profile (red and blue points in in Fig. 2(b)).

3.6. Phase shift

The relative phases between the beams are optimally set when the overall sum of the N patterns results in a homogeneous illumination, to avoid losses of information about the object. The three beams in the illumination produce three carrier frequencies (and their conjugates) in the illumination pattern, each produced by the mutual interference between pairs of the beams. The optimal three relative phase shifts of the k-th pattern are given by:

$$\begin{cases} \Delta\varphi_{12}^{k} = k\frac{2\pi}{7} \\ \Delta\varphi_{23}^{k} = k\frac{4\pi}{7} \\ \Delta\varphi_{13}^{k} = k\frac{6\pi}{7} \end{cases} \tag{5}$$

and are indicated in Table 1

where the indexes 1, 2 and 3 refer to the pairs of beams coming out from the chip that produce that carrier component. We note that from pattern $k = 4$, we exploited the 2π periodicity of the phase to reduce the absolute value of the required phase shift, and consequently of the required electrical power delivered to the phase shifters.

Optics EXPRESS

Table 1. Optimal relative spatial phases of carrier components in the illumination pattern

k	$\Delta\varphi_{12}^k$	$\Delta\varphi_{23}^k$	$\Delta\varphi_{13}^k$
0	0	0	0
1	$\frac{2\pi}{7}$	$\frac{4\pi}{7}$	$\frac{6\pi}{7}$
2	$\frac{4\pi}{7}$	$\frac{8\pi}{7}$	$\frac{12\pi}{7}$
3	$\frac{6\pi}{7}$	$\frac{12\pi}{7}$	$\frac{18\pi}{7}$
4	$\frac{8\pi}{7}$	$\frac{2\pi}{7}$	$\frac{10\pi}{7}$
5	$\frac{10\pi}{7}$	$\frac{6\pi}{7}$	$\frac{16\pi}{7}$
6	$\frac{12\pi}{7}$	$\frac{10\pi}{7}$	$\frac{22\pi}{7}$

A procedure to measure the actual phase of each carrier component in a single image was developed based on the same technique as used to identify the overall carrier spatial frequency, magnitude and phases as part of the calibration and reconstruction process [3,9]. Here we calculate the cross correlation of a low-pass and a high-pass filtered copy of the image in frequency space. This reveals the carrier components present in the image as peaks in the cross-correlation image whose phases are φ_{ij}^k. Measuring across a set of seven images representing $k = 0$ to 6 lets us compute the measured values of relative phase $\Delta\varphi_{ij}^k$ corresponding to the target values shown in Table 1.

3.7. SIM reconstruction

The reconstruction of enhanced resolution images from the acquired SIM data follows the method described previously [9], which implements standard algorithms [3], optimized for processing hex-SIM data in a Python environment with GPU acceleration. The procedure is a two-stage process involving a first calibration stage that measures the spatial frequencies, amplitudes and absolute phase of the carrier components in a 7 frame ($k = 0$ to 6) data set. Calibration needs only to be repeated on the timescale of the stability of the illumination system. The second reconstruction phase implements a spatial up-sampling of the data, followed by separation and shifting of the different frequency bands in the image to their correct position given by the spatial frequency of the carriers. Reconstruction also implements low spatial frequency suppression to remove out-of-focus signals and Wiener filtering to suppress the amplification of noise artifacts.

4. Conclusions

We introduced an optical device for the generation of phase-controlled point sources, arranged on a circle, with azimuthal polarization. The chip, installed on the illumination port of a widefield microscope can be used as the light source for structured illumination, upgrading the system to a SIM microscope. Using three sources, a hex-SIM pattern can be efficiently formed and, dynamically controlling the phase of the chip's waveguides, we can spatially shift the illumination pattern over the field of view of a widefield microscope. Using this device, we achieved enhanced resolution in imaging biological sample slides.

The present chip opens new possibilities to generate multiple point-sources, with controlled phase. We have presented a device that works in the context of hexagonal SIM, with a pattern formed by 3-beam interference, but similar devices could be fabricated to create a modulated pattern with a variety of different SIM arrangements. As an example, by adding a fourth waveguide, which implies a small modification of the chip design, one could create a new two-dimensional pattern, which allows the reconstruction of SIM data with a 2 times resolution enhancement, with

the acquisition of only 5 images [17]. The rapid prototyping of the fabrication process would enable the construction of this and potentially many other N-beams SIM configurations. The 3D capability of FLM could be further used to create fully integrated systems, even without the need for additional optical fibers. Along the same line, a higher number of waveguides, controlled in phase and possibly in polarization and amplitude, are conceivable using the present technology, providing the flexibility to generate the patterns for 2D and 3D structured illumination microscopy.

Funding. H2020 Excellent Science (871124); H2020 Future and Emerging Technologies (801336).

Acknowledgments. The device fabrication was partially performed at PoliFAB, the micro- and nanofabrication facility of Politecnico di Milano (www.polifab.polimi.it). The authors would like to thank the PoliFAB staff for the valuable technical support. The authors acknowledge Dr G. Corrielli for useful discussions on polarization control.

Disclosures. MC, PP, FB, RO, MN, HG, AB have filed a patent that relates to some aspects of this work.

Data availability. Data underlying the results presented in this paper are not publicly available at this time but may be obtained from the authors upon reasonable request. A python plugin, for reconstruction of hex-SIM data, named napari-sim-processor is available for download in the napari hub (https://www.napari-hub.org/).

References

1. R. Heintzmann and T. Huser, “Super-resolution structured illumination microscopy,” Chem. Rev. **117**(23), 13890–13908 (2017).
2. M. A. A. Neil, R. Juškaitis, and T. Wilson, “Method of obtaining optical sectioning by using structured light in a conventional microscope,” Opt. Lett. **22**(24), 1905–1907 (1997).
3. M. G. Gustafsson, “Surpassing the lateral resolution limit by a factor of two using structured illumination microscopy,” J. Microsc. **198**(2), 82–87 (2000).
4. M. G. Gustafsson, “Nonlinear structured-illumination microscopy: wide-field fluorescence imaging with theoretically unlimited resolution,” Proc. Natl. Acad. Sci. **102**(37), 13081–13086 (2005).
5. P. Jouchet, C. Cabriel, N. Bourg, M. Bardou, C. Poüs, E. Fort, and S. Lévêque-Fort, “Nanometric axial localization of single fluorescent molecules with modulated excitation,” Nat. Photonics **15**(4), 297–304 (2021).
6. B. C. Chen, W. R. Legant, K. Wang, L. Shao, D. E. Milkie, M. W. Davidson, and E. Betzig, “Lattice light-sheet microscopy: imaging molecules to embryos at high spatiotemporal resolution,” Science **346**(6208), 1257998 (2014).
7. L. Reymond, J. Ziegler, C. Knapp, F. C. Wang, T. Huser, V. Ruprecht, and S. Wieser, “SIMPLE: Structured illumination based point localization estimator with enhanced precision,” Opt. Express **27**(17), 24578–24590 (2019).
8. R. Förster, H. W. Lu-Walther, A. Jost, M. Kielhorn, K. Wicker, and R. Heintzmann, “Simple structured illumination microscope setup with high acquisition speed by using a spatial light modulator,” Opt. Express **22**(17), 20663–20677 (2014).
9. H. Gong, W. Guo, and M. A. Neil, “GPU-accelerated real-time reconstruction in Python of three-dimensional datasets from structured illumination microscopy with hexagonal patterns,” Phil. Trans. R. Soc. A **379**(2199), 20200162 (2021).
10. M. Žurauskas, I. M. Dobbie, R. M. Parton, M. A. Phillips, A. Göhler, I. Davis, and M. J. Booth, “IsoSense: frequency enhanced sensorless adaptive optics through structured illumination,” Optica **6**(3), 370–379 (2019).
11. V. d. Eynde, R. Vandenberg, W. Hugelier, S. Bouwens, A. Hofkens, J. Müller, and M. Dedecker, “Self-contained and modular structured illumination microscope,” Biomed. Opt. Express **12**(7), 4414–4422 (2021).
12. T. A. Hinsdale, S. Stallinga, and B. Rieger, “High-speed multicolor structured illumination microscopy using a hexagonal single mode fiber array,” Biomed. Opt. Express **12**(2), 1181–1194 (2021).
13. J. Pospíšil, G. Wiebusch, K. Fliegel, M. Klíma, and T. Huser, “Highly compact and cost-effective 2-beam super-resolution structured illumination microscope based on all-fiber optic components,” Opt. Express **29**(8), 11833–11844 (2021).
14. R. Osellame, H. J. Hoekstra, G. Cerullo, and M. Pollnau, “Femtosecond laser microstructuring: an enabling tool for optofluidic lab-on-chips,” Laser Photonics Rev. **5**(3), 442–463 (2011).
15. G. Corrielli, A. Crespi, R. Geremia, R. Ramponi, L. Sansoni, A. Santinelli, and R. Osellame, “Rotated waveplates in integrated waveguide optics,” Nat. Commun. **5**(1), 4249 (2014).
16. M. Calvarese, P. Paiè, F. Ceccarelli, A. Federico Sala, R. Bassi, F. Osellame, and Bragheri, “Strategies for improved temporal response of glass-based optical switches,” Sci. Rep. **12**(1), 239 (2022).
17. E. A. Ingerman, R. A. London, R. Heintzmann, and M. G. L. Gustafsson, “Signal, noise and resolution in linear and nonlinear structured-illumination microscopy,” J. Microsc. **273**(1), 3–25 (2019).
18. M. Schropp and R. Uhl, “Two-dimensional structured illumination microscopy,” J. Microsc. **256**(1), 23–36 (2014).
19. ØI Helle, F. T. Dullo, M. Lahrberg, J. C. Tinguely, O. G. Hellesø, and B. S. Ahluwalia, “Structured illumination microscopy using a photonic chip,” Nat. Photonics **14**(7), 431–438 (2020).
20. A. Descloux, K. S. Grußmayer, and A. Radenovic, “Parameter-free image resolution estimation based on decorrelation analysis,” Nat. Methods **16**(9), 918–924 (2019).

Optics EXPRESS

21. P. Paiè, R. Martínez Vázquez, R. Osellame, F. Bragheri, and A. Bassi, "Microfluidic based optical microscopes on chip," Cytometry **93**(10), 987–996 (2018).
22. F. Sala, M. Castriotta, P. Paiè, A. Farina, S. D'Annunzio, A. Zippo, R. Osellame, F. Bragheri, and A. Bassi, "High-throughput 3D imaging of single cells with light-sheet fluorescence microscopy on chip," Biomed. Opt. Express **11**(8), 4397–4407 (2020).
23. W. J. Chen, S. M. Eaton, H. Zhang, and P. R. Herman, "Broadband directional couplers fabricated in bulk glass with high repetition rate femtosecond laser pulses," Opt. Express **16**(15), 11470–11480 (2008).
24. G. Corrielli, S. Atzeni, S. Piacentini, I. Pitsios, A. Crespi, and R. Osellame, "Symmetric polarization-insensitive directional couplers fabricated by femtosecond laser writing," Opt. Express **26**(12), 15101–15109 (2018).
25. H. W. Lu-Walther, M. Kielhorn, R. Förster, A. Jost, K. Wicker, and R. Heintzmann, "fastSIM: a practical implementation of fast structured illumination microscopy," Methods Appl. Fluoresc. **3**(1), 014001 (2015).
26. F. Ceccarelli, S. Atzeni, A. Prencipe, R. Farinaro, and R. Osellame, "Thermal phase shifters for femtosecond laser written photonic integrated circuits," J. Lightwave Technol. **37**(17), 4275–4281 (2019).

131.175.28.29 {ts '2023-02-13 13:05:51'}